machines

MDPI

Article

An Asymmetric Independently Steerable Wheel for Climbing Robots and Its Motion Control Method

Meifeng Lv [1], Xiaoshun Liu [2], Lei Xue [1], Ke Tan [2], Junhui Huang [2] and Zeyu Gong [2,*]

[1] COMAC Shanghai Aircraft Manufacturing Co., Ltd., Shanghai 201324, China; lvmeifeng@comac.cc (M.L.); xuelei@comac.cc (L.X.)

[2] State Key Laboratory of Intelligent Manufacturing Equipment and Technology, School of Mechanical Science and Engineering, Huazhong University of Science and Technology, Wuhan 430074, China; m202170532@hust.edu.cn (X.L.); tanke@hust.edu.cn (K.T.); m202270537@hust.edu.cn (J.H.)

* Correspondence: gongzeyu@hust.edu.cn

Abstract: Climbing robots, with their expansive workspace and flexible deployment modes, have the potential to revolutionize the manufacturing processes of large and complex components. Given that the surfaces to be machined typically exhibit variable curvature, good surface adaptability, load capacity, and motion accuracy are essential prerequisites for climbing robots in manufacturing tasks. This paper addresses the manufacturing requirements of climbing robots by proposing an asymmetric independently steerable wheel (AISW) for climbing robots, along with the motion control method. Firstly, for the adaptability issue of the locomotion mechanism on curved surfaces under heavy load, an asymmetric independently steerable wheel motion module is proposed, which improves the steering difficulty of the traditional independently steerable wheel (ISW) based on the principle of steering assisted by wheels. Secondly, a kinematic model of the AISW chassis is established and, on this basis, a trajectory tracking method based on feedforward and proportional–integral feedback is proposed. Comparative experimental results on large, curved surface components show that the asymmetric independently steerable wheel has lower steering resistance and higher motion accuracy, significantly enhancing the reachability of climbing robots and facilitating their application in the manufacturing of large and complex components.

Keywords: climbing robot; independently steerable wheel; robot motion control

check for updates

Citation: Lv, M.; Liu, X.; Xue, L.; Tan, K.; Huang, J.; Gong, Z. An Asymmetric Independently Steerable Wheel for Climbing Robots and Its Motion Control Method. *Machines* **2024**, *12*, 536. https://doi.org/10.3390/machines12080536

Academic Editor: Hermes Giberti

Received: 2 July 2024
Revised: 23 July 2024
Accepted: 5 August 2024
Published: 6 August 2024

Copyright: © 2024 by the authors. Licensee MDPI, Basel, Switzerland. This article is an open access article distributed under the terms and conditions of the Creative Commons Attribution (CC BY) license (https://creativecommons.org/licenses/by/4.0/).

1. Introduction

Robotic intelligent manufacturing is the current trend in the production of large and complex components [1]. Climbing robots use various adhesion methods and movement mechanisms to operate on vertical structures, offering expansive workspaces and flexible deployment modes. These capabilities overcome the reachability limitations of traditional manufacturing methods, potentially revolutionizing the manufacturing processes of large and complex components [2]. In recent years, climbing robots have been applied in the aviation [3], marine engineering [4], energy [5], and construction industries [6], though their usage has been primarily limited to relatively simple tasks such as inspection and cleaning.

The surfaces of large and complex components are typically continuous freeform surfaces, making wheel-based motion mechanisms most suitable for climbing robots in manufacturing tasks. Currently, there is a rich variety of wheel-based motion mechanisms designed for climbing robots. Zhong et al. designed an omnidirectional mobile climbing robot that achieves omnidirectional movement on vertical surfaces using a chassis with three omnidirectional wheels [7]. Liu et al. developed a climbing robot for wind turbine maintenance that uses Mecanum wheels for flexible movement [8]. Huang et al. created a tracked climbing robot for ship inspection, which combines magnetic tracks and magnets to move on vertical and uneven surfaces [9]. GUO et al. proposed an underwater climbing and adhesion robot that uses independently steerable wheels. The robot's four independently

steerable wheels are driven by a single power source and synchronize through a specially designed transmission structure [10]. ETO et al. introduced a climbing robot with spherical magnetic wheels suitable for large steel structures. By adding two degrees of freedom to the magnetic adhesion wheels, the robot can adapt to surfaces with large curvature variations while ensuring the adhesion force is always perpendicular to the surface [11]. Inspired by the hook-climbing mechanism of *Galium aparine*, FIORELLO et al. designed a micro-patterned flexible wheel that can climb directly on slopes with an angle of 60° [12].

In wheel-based motion mechanisms, independently steerable wheels (ISWs) are most suitable for climbing robots in manufacturing tasks due to their excellent grip capacity and flexibility on curved surface. ISWs possess the following two degrees of freedom: the rotation of the driving wheel and the rotation of the steering mechanism, which provide independent steering capacity, respectively. ISWs are widely used and extensively studied in the field of robotics. There is substantial research on both the motion models and control methods of independently steerable wheel mobile robots.

In terms of motion models, distinct kinematic and dynamic models are built regarding different numbers of wheels. Most existing studies focus on four-wheel configurations. For instance, Beomsu et al. designed a four-independently steerable mobile robot with adaptive steering capabilities [13]. Li et al. implemented online kinematic model parameter estimation for motion trajectory tracking in a four-wheel skid-steering robot [14]. Xu et al. achieved path tracking for a four-wheel independently steerable and independently driven agricultural machinery based on variable preview distance [15]. Additionally, Xu et al. designed a five-wheel mobile robot that solves the issue of continued movement after flipping by configuring different wheelbases, track widths, and center-of-gravity heights [16].

Regarding control methods, there are various control strategies for ISWs, including Model Predictive Control (MPC), fuzzy control, PID control, and sliding mode control. For example, Ding et al. achieved trajectory tracking for redundantly driven mobile robots using MPC for speed control [17]. Liu et al. proposed a high-speed trajectory tracking control method based on MPC, applied to four-wheel independently steerable robots [18]. In fuzzy control, Kato et al. employed an image-based fuzzy control method for straight trajectory tracking control of four-wheel steerable mobile robots [19]. Tan et al. proposed a cascade direct yaw moment control strategy based on PID control, using dual PID controllers to enhance the path tracking accuracy and stability of the ISWs [20]. Gao et al. introduced a steering control strategy for a greenhouse spraying mobile robot based on dynamic sliding mode control, achieving stable steering control in complex environments by using slip angle and yaw rate as combined control variables [21].

In summary, existing research on ISWs predominantly focuses on mobile robots on flat horizontal planes, showcasing their advantages in high-precision motion control. However, there is a scarcity of studies on the application of ISWs on variable curvature vertical surfaces. Particularly in the specific working conditions of climbing robots, traditional ISWs may encounter the problem of steering jamming. This issue manifests when the steering mechanism cannot overcome the rotational resistance and remains stationary during specialized operations. Traditional ISWs are symmetrically arranged, meaning the rotation center of the driving wheel is at the midpoint of the contact line between the driving wheel and the ground when the steering mechanism rotates. During in-place steering motion of climbing robots with ISWs, each driving wheel experiences sliding friction with the curved surface since the driving wheel speed is zero while the steering mechanism speed is non-zero, which may lead to jamming.

The jamming of ISWs is primarily due to the following two reasons: Firstly, climbing robots require significant adhesion force to maintain attachment, which greatly increases the frictional resistance between the wheel and the curved surface, which, in turn, causes a heavy load for the steering mechanism. Secondly, climbing robots operate on curved surfaces, where the steering mechanism must also overcome a portion of the support force when rotating on the surface.

To address the above issues of the traditional ISWs, this paper proposes an asymmetric ISW (AISW) motion mechanism for climbing robots. The AISW mechanism's steering is assisted by the driving wheel, which converts sliding friction into rolling friction, thereby significantly reducing the rotational resistance of the steering mechanism and enabling flexible rotation. A trajectory tracking method for the climbing robot equipped with the AISW based on feedforward and proportional–integral feedback is then proposed. Comparative experiments on surface motion demonstrate that the proposed AISW and its corresponding control method can effectively improve the motion performance of climbing robots on curved surfaces.

The subsequent sections of this paper are arranged as follows: Section 2 introduces the mechanical structure of the AISW and the speed control method of the driving wheel. Section 3 presents the trajectory tracking method for the chassis with the AISW. Section 4 describes the steering experiments and trajectory tracking experiments of the asymmetric ISWs. Section 5 concludes the work of this paper.

2. Asymmetric Independently Steerable Wheel

To prevent steering jamming in traditional ISWs, we have designed an AISW mechanism, which is assisted by the driving wheel. This section first discusses the structure and theoretical analysis of the AISWs, followed by an introduction to the control method for the proposed mechanism.

2.1. Structure and Theoretical Analysis of the AISW

The proposed ASIW, as shown in Figure 1, includes a driving motor (1), a steering motor (2), a bearing platform (3), a steering mechanism (4), a driving wheel axle (5), a driving wheel (6), and a wheel axle mounting seat (7).

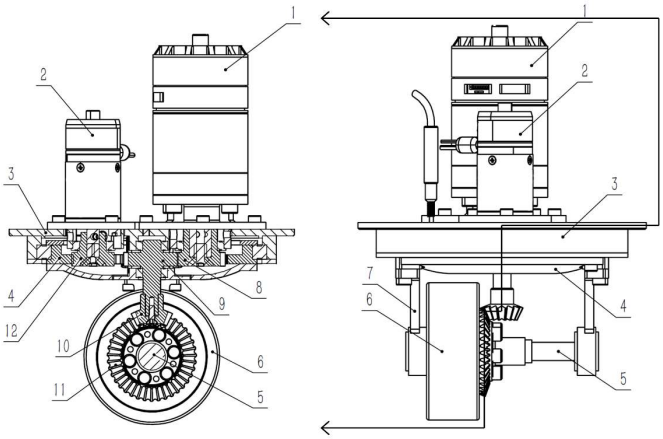

Figure 1. Schematic Diagram of the AISW.

In this AISW, the bearing platform is fixedly connected to the robot chassis, and both the driving motor and the steering motor are fixed on the bearing platform. The steering motor drives the steering mechanism to rotate through a spur gear (12) and an internal gear ring of the steering mechanism. The driving motor drives the wheel through two spur gears (8, 9) and two bevel gears (10, 11), so the output shaft of the driving motor is perpendicular to the chassis and parallel to the output shaft of the steering motor. During steering operations, the driving motor, steering motor, and bearing platform remain stationary and thus can be treated as a fixed unit; meanwhile, the steering mechanism, wheel axle mounting seat, and driving wheel will remain relative stationary and temporarily form a rotating unit, rotating together to change the heading.

The primary reasons for jamming of ISWs are twofold. Firstly, the driving wheels cannot coordinate with the steering mechanism rotation, and the steering mechanism must overcome the maximum static friction between the driving wheel and the ground,

leading to jamming, as shown in Figure 2. Secondly, when the climbing manufacturing robot operates on curved surfaces, the ISWs may partially lift off the surface. When the steering mechanism rotates on a curved surface, it also needs to overcome a component of the support force, as shown in Figure 3. In the figure, the ISW has rotated 90°, with (a) representing the initial state and (b) the final state. In (a), the axis of the steering mechanism rotation is not parallel to the surface normal. The support force F_N acts along the surface normal, with a component F_{Nx} in the plane of the steering mechanism rotation that hinders its movement. Therefore, when the steering mechanism is in state (a), it must also overcome a component of the support force, making it prone to jamming. Additionally, during steering on curved surfaces, traditional ISWs may rotate around the main contact point due to partial lift-off, causing misalignment, as shown in Figure 4.

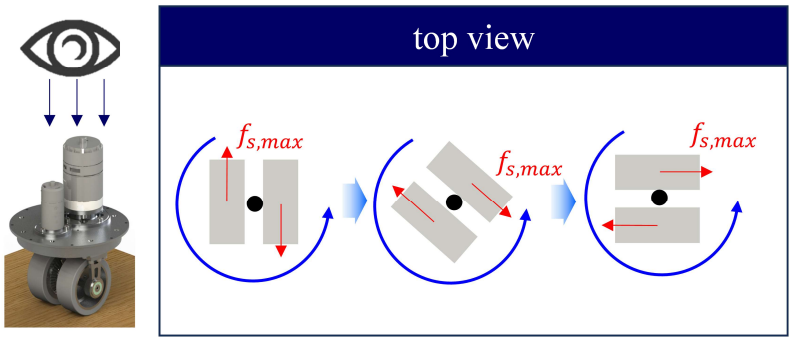

Figure 2. Diagram of Variables for the ISW.

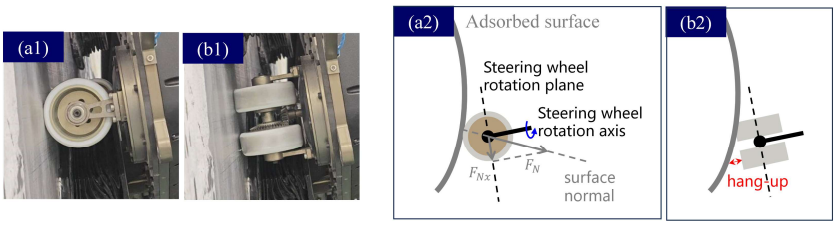

Figure 3. Traditional ISWs need to overcome support force components during steering. (**a**) Initial state. (**b**) Final state.

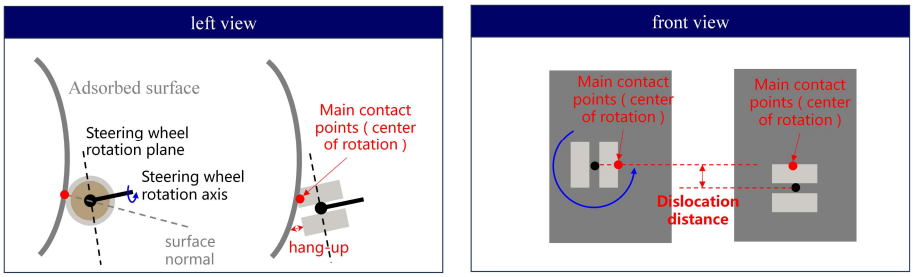

Figure 4. Traditional ISWs exhibit misalignment during steering.

In contrast, the AISWs proposed in this paper can significantly reduce the rotational resistance of the steering mechanism by converting sliding friction into rolling friction, as the driving wheels coordinate with the steering mechanism rotation. The driving wheels also assist in overcoming the support force component. Moreover, since the driving wheels coordinate with the steering mechanism rotation, the rotation center is the center of the steering mechanism, preventing misalignment of the ISWs. This approach addresses the jamming and misalignment issues faced by the ISWs.

2.2. Control Method for the AISW

Due to the bevel gear transmission, the rotation of the steering motor also causes the driving wheel to rotate. A typical scenario is when the driving motor outputs zero speed, and the steering motor outputs a certain speed to rotate the steering mechanism, causing the driving wheel to rotate, as shown in Figure 5a. This means that the rotational speed of the driving wheel is not solely determined by the driving motor but by the combined effect of the driving motor and the steering motor. The relationship between the steering mechanism speed, driving wheel speed, and the driving motor and steering motor can be described as below:

$$\dot{\delta} = i_{dir}^{m}\omega_{dir}^{m} \tag{1}$$

$$\omega_{drv} = i_{drv}^{m}\omega_{drv}^{m} + i_{cone}\dot{\delta} \tag{2}$$

where:

δ: steering angle of the steering mechanism.
$\dot{\delta}$: angular velocity of the steering mechanism.
i_{dir}^{m}: transmission ratio from the steering motor to the steering mechanism.
ω_{dir}^{m}: angular velocity of the steering motor output shaft.
ω_{drv}: angular velocity of the driving wheel around the driving wheel axle (5).
i_{drv}^{m}: transmission ratio from the driving motor to the driving wheel.
ω_{drv}^{m}: angular velocity of the driving motor output shaft.
i_{cone}: transmission ratio of the bevel gears (10, 11).

According to (2), when the steering mechanism rotates, to ensure the speed of the driving wheel around the driving wheel axle is zero, the angular speed of the driving motor needs to be set to a specific value, as shown in Figure 5b.

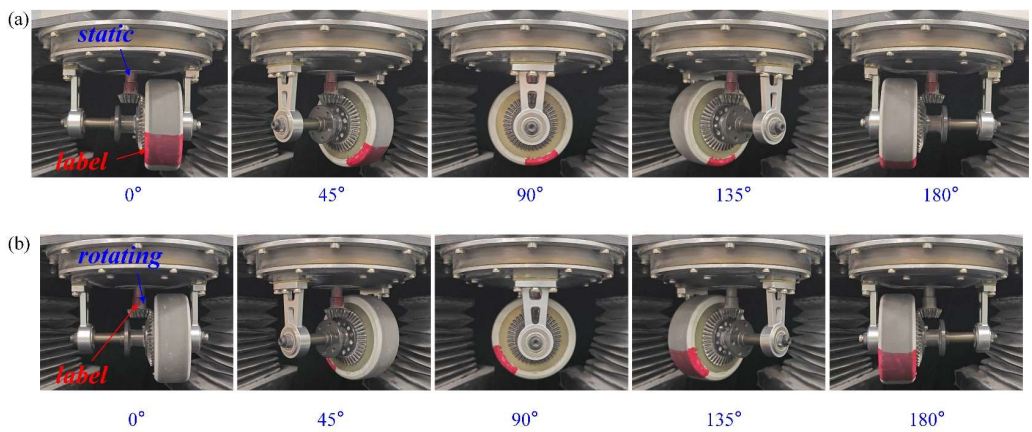

Figure 5. The rotation state of driving wheels jointly determined by the driving motor and steering motor. The red label on the wheel is used to indicate the rotating direction of the driving wheel. (**a**) The driving wheel's rotation is caused by the bevel gear transmission and steering motor. (**b**) The driving wheel remains static when a compensating speed is given.

The specific driving method is as follows:

The basic idea is to add the angular velocity of the steering mechanism to the speed of the driving wheels, ensuring that the lower end of the driving wheels maintains zero velocity in the world coordinate system. As shown in Figure 6, during one complete rotation of the steering mechanism, the rolling direction of the driving wheels matches the rotation direction of the steering mechanism.

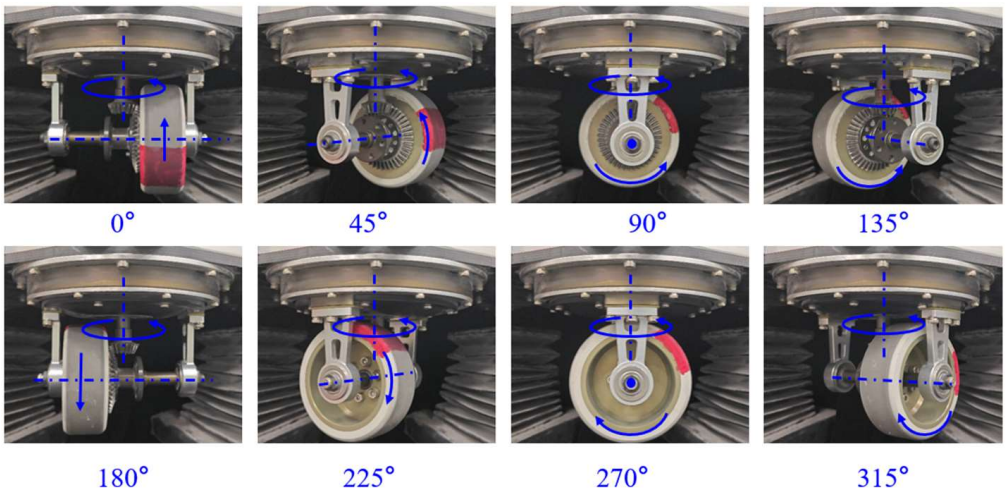

Figure 6. Coordination of the driving wheel and steering mechanism rotation in AISW.

The principle of coordinating the driving wheel with the steering mechanism in the AISW is to ensure that point W on the tire tread (see Figure 7), which is the distal point on the contact line between the wheel and the curved surface, remains stationary relative to the world coordinate system.

$$v_V^W = 0 \tag{3}$$

where v_V^W is the velocity of point W on the tire tread in the world coordinate system.

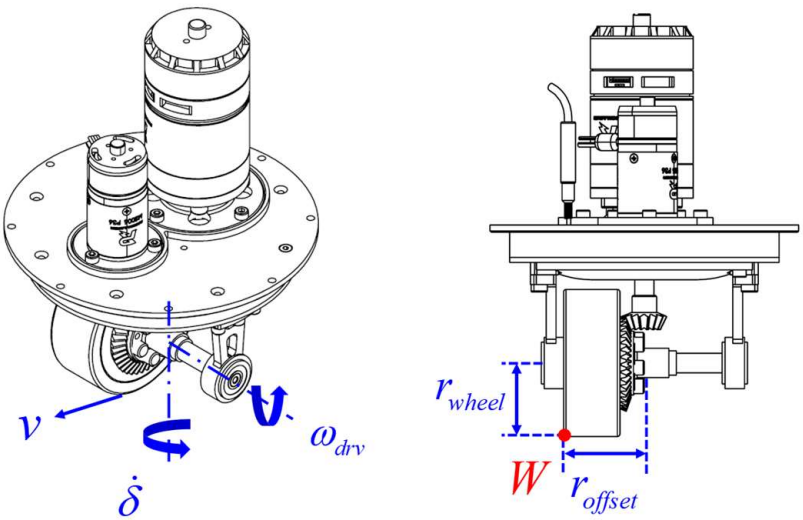

Figure 7. Diagram of Variables for the AISW, where v represents the linear velocity of the wheel, ω_{drv} represents the angular velocity of the driving wheel, $\dot{\delta}$ represents the steering angular velocity of the wheel, W represents a point on the tire tread, r_{wheel} represents the radius of the driving wheel and r_{offset} represents the distance from point W to the rotation center of the steering mechanism.

From relative motion, the velocity of point W on the wheel relative to the robot chassis equals the rotational speed of the wheel around its axle plus the rotational speed caused by the steering mechanism. Here, v is the velocity of point W on the tire tread relative to the robot chassis, r_{wheel} is the radius of the driving wheel, and r_{offset} is the distance from point W to the rotation center of the steering mechanism.

$$v = \omega_{drv} r_{wheel} + \dot{\delta} r_{offset} \tag{4}$$

From relative motion, the velocity of point W on the tire tread in the world coordinate system v_V^W is the sum of the velocity of point W on the tire tread relative to the robot chassis and the velocity of the coinciding point on the robot chassis in the world coordinate system. Here, $v_{robot,V}^W$ is the velocity of the coinciding point on the robot chassis in the world coordinate system.

$$v_V^W = v + v_{robot,V}^W \tag{5}$$

Assuming no lateral slippage of the wheel, combining Equations (2)–(5), we can derive the angular velocity of the driving motor output shaft ω_{drv}^m as follows:

$$\omega_{drv}^m = -\frac{1}{i_{drv}^m r_{wheel}}(i_{cone} r_{wheel}\dot{\delta} + r_{offset}\dot{\delta} + v_{robot,V}^W) \tag{6}$$

Equation (6) reflects the method for regulating the angular velocity of the driving motor. The right side of the equation includes three additive terms. The first term reflects the influence of the bevel gear transmission, the second term reflects the coordination of the driving wheel with the steering mechanism rotation, and the third term is the velocity of the coinciding point on the robot chassis in the world coordinate system. It reflects the driving effect of the AISW on the robot.

Compared to ω_{drv}^m, $v_{robot,V}^W$ more accurately represents the direct control of the robot chassis by the AISW. Therefore, in the motion control of the robot, this paper considers $v_{robot,V}^W$ as the control variable for the robot's motion, referred to as the wheel speed. After the wheel speed is determined, ω_{drv}^m can be calculated using Equation (6).

In conclusion, the AISW using this speed regulation method mainly experiences rolling friction during the in-place steering motion. This characteristic results in lower steering resistance and higher motion accuracy compared to traditional ISWs.

3. Trajectory Tracking Method for the Climbing Robot with AISW

This section describes the kinematic model of the climbing robot with AISWs. Based on this, a trajectory tracking controller based on feedforward and proportional–integral feedback is proposed.

3.1. Kinematic Model of the Chassis with AISW

The designed chassis for the climbing robot contains three AISWs which are symmetrically distributed around the center of the chassis. As shown in Figure 8, to describe the omnidirectional movement of the robot, a global coordinate system $\{X^W O^W Y^W\}$, a robot coordinate system $\{X^R O^R Y^R\}$, and independently steerable wheel coordinate systems $\{x^i o^i y^i\}$ are established in the robot system. i represents the ith AISW. The forward direction of the robot body, when the steering angles of all the steering mechanisms are zero, is taken as the x-axis of $\{X^R O^R Y^R\}$ and $\{x^i o^i y^i\}$. x^W and y^W are the positions of the robot in the global coordinate system, and θ is the robot's orientation in the global coordinate system. V^R is the linear velocity of the robot in the robot coordinate system, with V_x^R and V_y^R being its components along the x and y axes, respectively.

The wheels are symmetrically distributed around the center of the robot, and each wheel is equidistant from the robot's center, with R being the distance from a wheel to the robot's center. The positions of the three independently steerable wheel centers in the robot coordinate system are $(x_1, y_1) = (R, 0)$, $(x_2, y_2) = (-\frac{R}{2}, \frac{\sqrt{3}R}{2})$, and $(x_3, y_3) = (-\frac{R}{2}, -\frac{\sqrt{3}R}{2})$. Here, v_i and $\dot{\delta}_i$ represent the velocity of point W on the wheel i (Figure 7) relative to the chassis, v_i being the linear velocity of wheel i, $\dot{\delta}_i$ being the steering angular velocity of wheel i, and δ_i being the steering angle of the steering mechanism of driving wheel i. b is the eccentricity of the AISW, specifically the distance from point W to the rotation center of the steering mechanism in Figure 7, and φ_i is the angle between point W on wheel i and the x-axis of the independently steerable wheel coordinate system, where:

$$\varphi_i = \delta_i - \frac{\pi}{2} \tag{7}$$

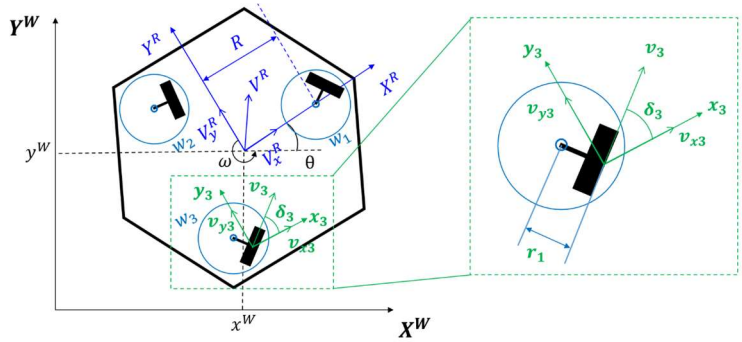

Figure 8. Kinematic model of the climbing robot with AISW, where the black coordinate system represents the world coordinate system $\{X^W O^W Y^W\}$, the blue coordinate system represents the robot coordinate system $\{X^R O^R Y^R\}$, and the green coordinate system represents the independently steerable wheel coordinate system $\left\{x^i o^i y^i\right\}$, with i representing the ith AISW.

3.2. Forward and Inverse Kinematics of the Climbing Robot with AISWs

The velocity of the robot's center in the world coordinate system $\begin{bmatrix}\dot{X}^W & \dot{Y}^W & \dot{\theta}\end{bmatrix}^T$ is considered the robot's state $[v_1\ v_2\ v_3\ \delta_1\ \delta_2\ \delta_3]^T$, and the steering angles and wheel speeds of the ISWs are the control inputs denoted as U. Assuming no slippage of the wheels, the robot's forward and inverse kinematics relationship between $\dot{X}$ and U can be derived.

V^R is the robot's linear velocity in the robot coordinate system, and its relationship with $\dot{X}$ is given by the following:

$$\begin{bmatrix} V_x^W \\ V_y^W \end{bmatrix} = M \begin{bmatrix} V_x^R \\ V_y^R \end{bmatrix} \tag{8}$$

$$M = \begin{bmatrix} \cos(\theta) & -\sin(\theta) \\ \sin(\theta) & \cos(\theta) \end{bmatrix} \tag{9}$$

Assuming no slippage of the wheels, the robot's motion in the robot coordinate system satisfies the following relationship:

$$\begin{bmatrix} v_{xi} \\ v_{yi} \end{bmatrix} = \begin{bmatrix} V_x^R \\ V_y^R \end{bmatrix} + \omega \times \overrightarrow{O^R W_i} \tag{10}$$

where:

$$\begin{bmatrix} v_{xi} \\ v_{yi} \end{bmatrix} = \begin{bmatrix} v_i \cos(\delta_i) \\ v_i \sin(\delta_i) \end{bmatrix} \tag{11}$$

$$\omega \times \overrightarrow{O^R W_i} = \begin{bmatrix} 0 & -\omega \\ \omega & 0 \end{bmatrix} \overrightarrow{O^R W_i} \tag{12}$$

Here, ω is the angular velocity of the robot, $\omega = \dot{\theta}$, W_i is the distal point on the contact line between the wheel i and the ground, O^R is the origin of the robot coordinate system, i.e., the center position of the robot.

From geometric relationships, we can derive the following:

$$\overrightarrow{O^R W_i} = \overrightarrow{O^R o^i} + \overrightarrow{o^i W_i} \tag{13}$$

where:

$$\overrightarrow{O^R o^i} = \begin{bmatrix} x_i \\ y_i \end{bmatrix} \tag{14}$$

$$\overrightarrow{o^i W_i} = \begin{bmatrix} b\cos(\varphi_i) \\ b\sin(\varphi_i) \end{bmatrix} \tag{15}$$

and where o^i is the center of the independently steerable wheel i.

By combining Equations (7)–(15), the kinematic equations of the robot can be derived as follows:

$$A \begin{bmatrix} v_1 \\ v_2 \\ v_3 \end{bmatrix} = BM^{-1} \begin{bmatrix} \dot{X}^W \\ \dot{Y}^W \\ \dot{\theta} \end{bmatrix} \tag{16}$$

$$A = \begin{bmatrix} c(\delta_1) & 0 & 0 \\ s(\delta_1) & 0 & 0 \\ 0 & c(\delta_2) & 0 \\ 0 & s(\delta_2) & 0 \\ 0 & 0 & c(\delta_3) \\ 0 & 0 & s(\delta_3) \end{bmatrix} \tag{17}$$

$$B = \begin{bmatrix} 1 & 0 & bc(\delta_1) - y_1 \\ 0 & 1 & bs(\delta_1) + x_1 \\ 1 & 0 & bc(\delta_2) - y_2 \\ 0 & 1 & bs(\delta_2) + x_2 \\ 1 & 0 & bc(\delta_3) - y_3 \\ 0 & 1 & bs(\delta_3) + x_3 \end{bmatrix} \tag{18}$$

where $\mathrm{c}(\theta)$ is $\cos(\theta)$ and $\mathrm{s}(\theta)$ is $\sin(\theta)$.

Thus, the robot's forward kinematics $\dot{X} = f_{3WIS}(U)$ are as follows:

$$\begin{bmatrix} \dot{X}^W \\ \dot{Y}^W \\ \dot{\theta} \end{bmatrix} = \mathrm{M}B^{-1}A \begin{bmatrix} v_1 \\ v_2 \\ v_3 \end{bmatrix} \tag{19}$$

The inverse kinematics of the robot have two sets of solutions, one of which is the following:

$$v_i = -\omega b + \sqrt{\left(V_x^W \mathrm{c}(\theta) + V_y^W \mathrm{s}(\theta) - \omega y_i\right)^2 + \left(V_y^W \mathrm{c}(\theta) - V_x^W \mathrm{s}(\theta) + \omega x_i\right)^2} \tag{20}$$

$$\delta_i = \mathrm{arctan2}(V_y^W \mathrm{c}(\theta) - V_x^W \mathrm{s}(\theta) + \omega x_i, V_x^W \mathrm{c}(\theta) + V_y^W \mathrm{s}(\theta) - \omega y_i) \tag{21}$$

The other set is as follows:

$$v_i = -\omega b - \sqrt{\left(V_x^W \mathrm{c}(\theta) + V_y^W \mathrm{s}(\theta) - \omega y_i\right)^2 + \left(V_y^W \mathrm{c}(\theta) - V_x^W \mathrm{s}(\theta) + \omega x_i\right)^2} \tag{22}$$

$$\delta_i = \mathrm{arctan2}(V_y^W \mathrm{c}(\theta) - V_x^W \mathrm{s}(\theta) + \omega x_i, V_x^W \mathrm{c}(\theta) + V_y^W \mathrm{s}(\theta) - \omega y_i) + \pi \tag{23}$$

The reason for having two sets of solutions is that rotating the steering angle of the ISW by 180° and flipping the wheel can achieve the same effects.

3.3. Trajectory Tracking Method Based on Feedforward and Proportional–Integral Feedback

The trajectory of a climbing robot consists of trajectory points spaced 1 mm apart. The schematic diagram and block diagram of the controller are shown in Figures 9 and 10, respectively. $\dot{X}_U$ is composed of linear velocity V_{out} and angular velocity ω_{out}.

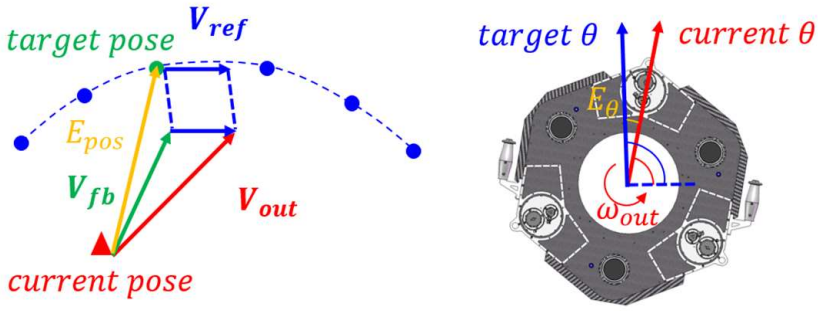

Figure 9. Schematic diagram of acquiring desired linear velocity and angular velocity in the trajectory tracking controller.

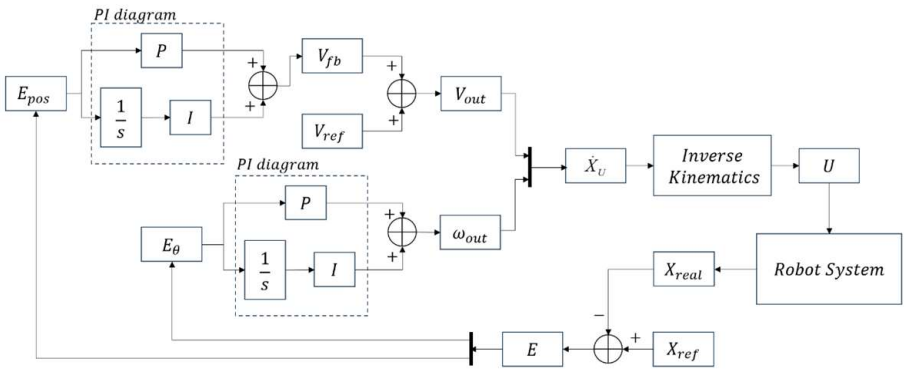

Figure 10. Block diagram of the trajectory tracking controller.

The linear velocity V_{out} is composed of a feedforward velocity V_{ref} and a feedback velocity V_{fb}. The feedforward velocity is a pre-planned velocity, with direction along the tangent of the trajectory. The feedback velocity is obtained by adding the proportional and integral of the position error E_{pos}.

On the other hand, the angular velocity ω is obtained by adding the proportional and integral of the angle error E_θ. Once $\dot{X}_U$ is obtained, the steering angles and wheel speeds of the ISWs U are calculated using the inverse kinematics Equations (20)–(23). Finally, U is input into the robot system.

Simultaneously, the robot's actual pose X_{real} is acquired by the robot's localization module. The pose error E is the difference between the target pose X_{ref} and the actual pose X_{real}. The pose error includes the position error E_{pos} and the angle error E_θ.

4. Experiment

This section presents two sets of experiments. The first set compares the steering current between the AISW and traditional ISW to demonstrate that the AISW mechanism can effectively prevent steering jamming. The second set involves trajectory tracking experiments of climbing robots equipped with AISWs on a thin-walled skin and a wind turbine blade. These experiments validate the effectiveness of the trajectory tracking control method designed for the AISW.

4.1. Climbing Robot Platform

The climbing robot platform used in the experiments is shown in Figure 11. The climbing robot weighs 14 kg and has a hexagonal shape with a length of approximately 0.7 m. It primarily consists of three ISW evenly distributed on the robot's chassis and three evenly distributed flexible adsorption chambers.

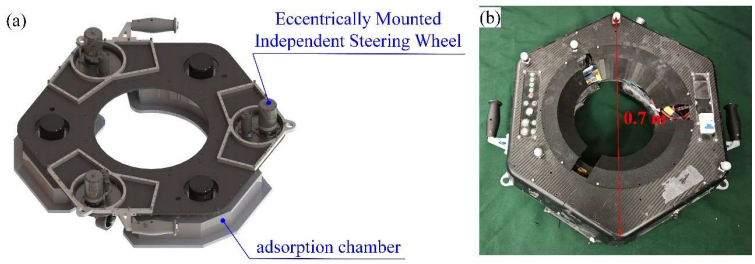

Figure 11. Climbing robot platform. (**a**) Chassis of the climbing robot. (**b**) Climbing robot prototype.

The adsorption chambers are driven by centrifugal fans, generating negative pressure within the chambers. This applies pressure to the robot, allowing it to adhere to and move along curved surfaces.

Two different types of steering wheels are equipped on the climbing robot platform, as shown in Figure 12. These include the traditional ISWs and the proposed AISWs. The wheels have a diameter of 0.06 m, and the driving wheels and steering mechanisms are driven by DC motors, respectively. The treads of the wheels are made of polyurethane to generate sufficient friction for the robot's movement on curved surfaces.

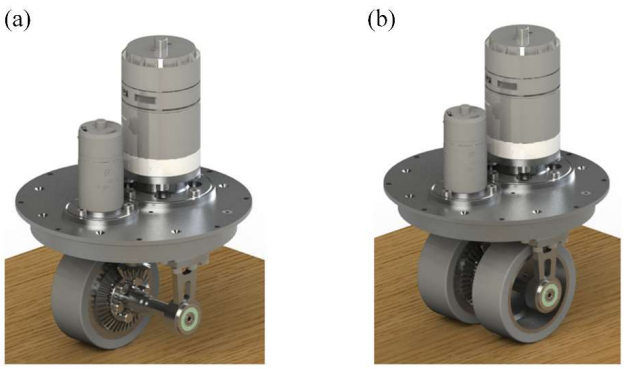

Figure 12. Steering wheels. (**a**) Proposed AISWs. (**b**) Traditional ISWs.

4.2. Comparison Experiment of Steering Current between AISW and Traditional ISW

Since the driving wheels of the AISWs can coordinate with the rotation of the steering mechanism, the AISWs can more easily adjust the steering angle direction compared to symmetrical ISWs. This section conducts a comparison experiment between the AISWs and the traditional ISWs. As shown in Figure 13, the experimental platform includes a thin-walled skin, a robot with AISWs, and a climbing robot with traditional ISWs. The experiment involves attaching the climbing robot to the thin-walled skin and execute the in-place steering motion.

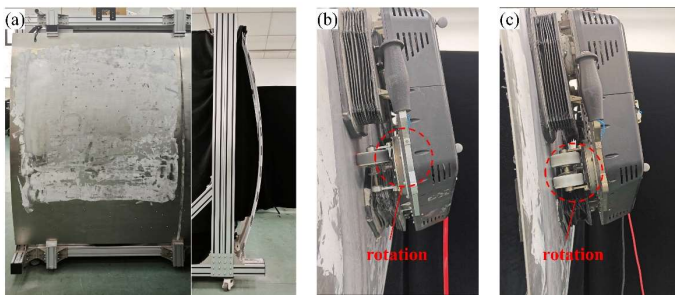

Figure 13. Climbing robot platform adheres to the thin-walled skin and performs in-place steering motions. (**a**) Thin-walled skin. (**b**) Climbing robot equipped with proposed AISWs. (**c**) Climbing robot equipped with traditional ISWs.

To validate the effectiveness of the proposed AISW, the currents of the driving motor and the steering motor are measured and recorded for evaluating the rotational resistance on the steering mechanism. The recorded current data are shown in Figure 14. Figure 14a shows the current of the steering motors, while Figure 14b shows the current of the driving motors. From the figures, it can be seen that during the in-place rotation of the wheels, the current of the steering motors for the AISWs is significantly lower than that of the traditional ISWs. This indicates that the AISWs considerably reduce the resistance during the in-place rotation. Additionally, as analyzed in Section 2, to achieve in-place rotation without movement, the drive motors need to be compensated with an appropriate speed, resulting in varying drive motor currents. As shown in Figure 14b, the driving motor current for the proposed AISWs is also significantly lower than that for the ISWs.

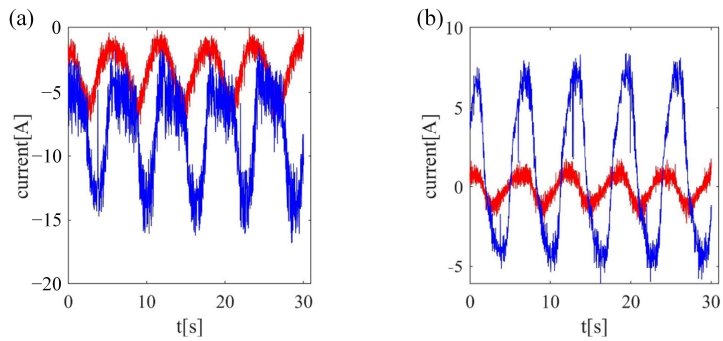

Figure 14. Currents of steering motor and driving motor during in-place steering. (**a**) Steering motor current of the AISWs (red), steering motor current of the traditional ISWs (blue). (**b**) Driving motor current of the AISWs (red), driving motor current of the traditional ISWs(blue).

The statistical analysis of the experimental results is shown in Table 1. It can be seen that the root mean square (RMS) current of the steering motor for the AISW is 42% of that for the ISW. The maximum current of the steering motor for the AISW is 45% of that for the ISW. The RMS current of the driving motor for the AISW is only 18% of that for the ISW, and the maximum current of the driving motor for the AISW is 30% of that for the ISW. It is evident that the rotational resistance of the AISWs is significantly reduced in comparison with that of the ISWs.

Table 1. Average and maximum currents of steering motor and driving motor during in-place rotation.

	AISW	**ISW**
Steering Motor RMS Current [A]	3.7802	8.9760
Steering Motor Maximum Current [A]	7.4740	16.7740
Driving motor RMS Current [A]	0.7933	4.4007
Driving motor Maximum Current [A]	2.5340	8.4240

4.3. Trajectory Tracking Experiment of Climbing Robot with AISWs

To validate the effectiveness of the trajectory tracking control based on feedforward and proportional–integral (PI) feedback, trajectory tracking experiments were conducted. The experimental platform, as shown in Figure 15, includes a climbing robot, a thin-walled skin, a wind turbine blade, and the OptiTrack motion capture system. The thin-walled skin is 1.2 m wide, 1.8 m high, and has a minimum curvature radius of about 1.5 m. The wind turbine blade is approximately 6 m long and 3.6 m high. The experimental sites for both the thin-walled skin and the wind turbine blade are covered by OptiTrack motion capture cameras, which are mounted on a truss. Specifically, each position the robot passes through can be seen by at least two motion capture cameras. This OptiTrack system can provide real-time three-dimensional pose data for the robot with a position measurement accuracy of 0.1 mm.

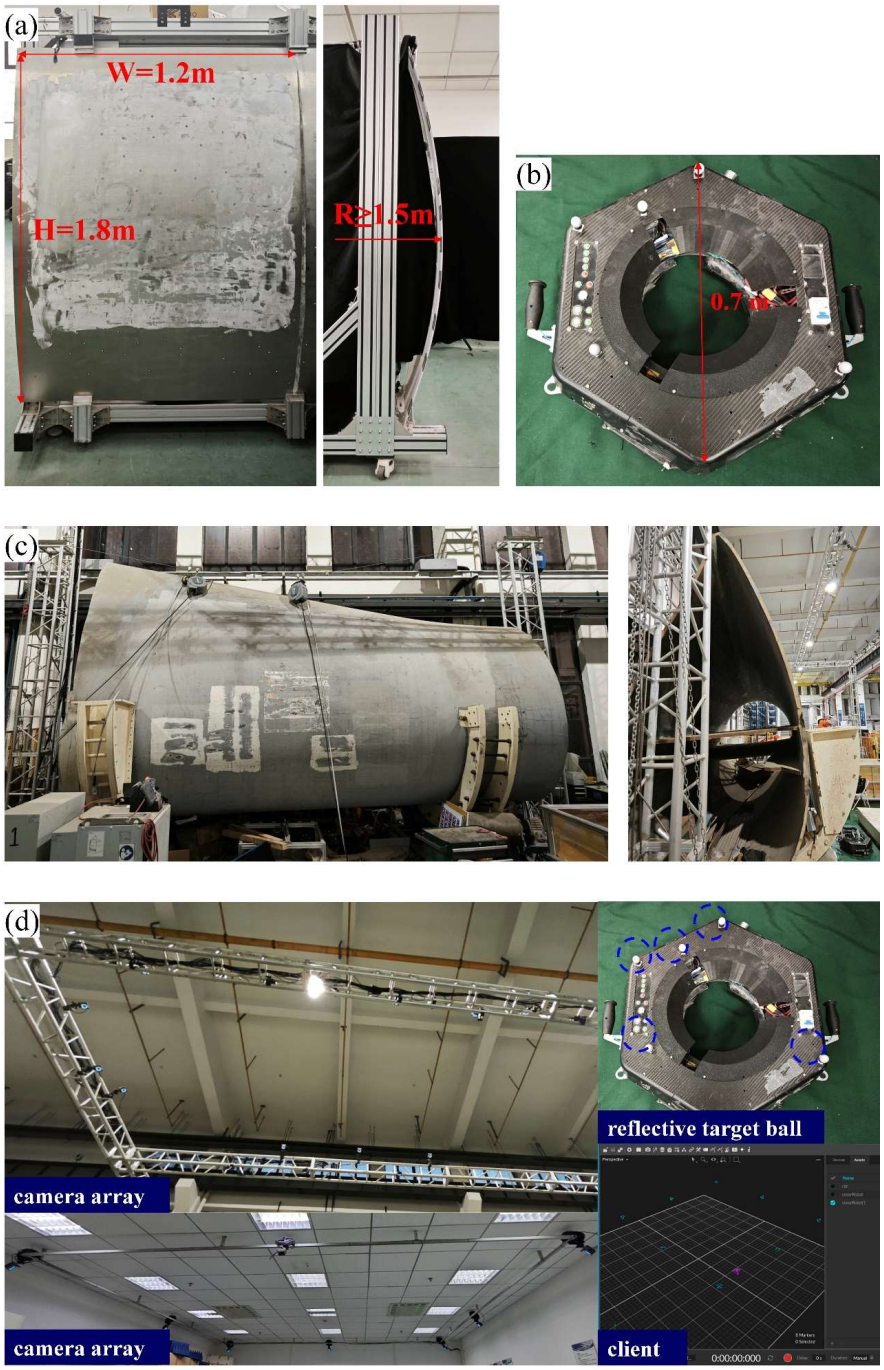

Figure 15. Trajectory tracking experimental platform. (**a**) Thin-walled skin. (**b**) Climbing manufacturing robot. (**c**) Wind turbine blade. (**d**) OptiTrack motion capture system.

Using the trajectory tracking controller based on feedforward and proportional–integral (PI) feedback, straight and curved trajectories are tracked on the thin-walled skin and wind turbine blade. During the trajectory tracking process, data such as the actual pose, target pose, and intermediate variables of the algorithm are recorded, and the trajectory tracking accuracy is ultimately evaluated. The trajectory diagram on the thin-walled skin is shown in Figure 16. The straight trajectory is a square with a side length of 0.4 m, and the curved trajectory is a circle with a diameter of 0.4 m. The trajectory diagram on the wind turbine blade is shown in Figure 17. The straight trajectory is a rectangle with a length of 2.5 m and a width of 1 m, and the curved trajectory is a circle with a diameter of 1 m.

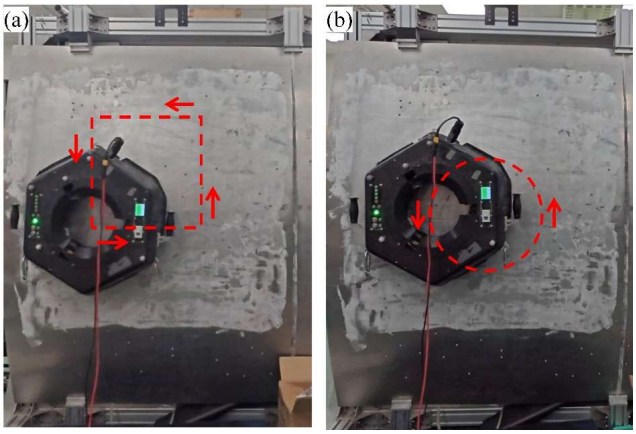

Figure 16. Trajectory diagram on the thin-walled skin. (**a**) A square trajectory with a side length of 0.4 m. (**b**) A circle trajectory with a diameter of 0.4 m.

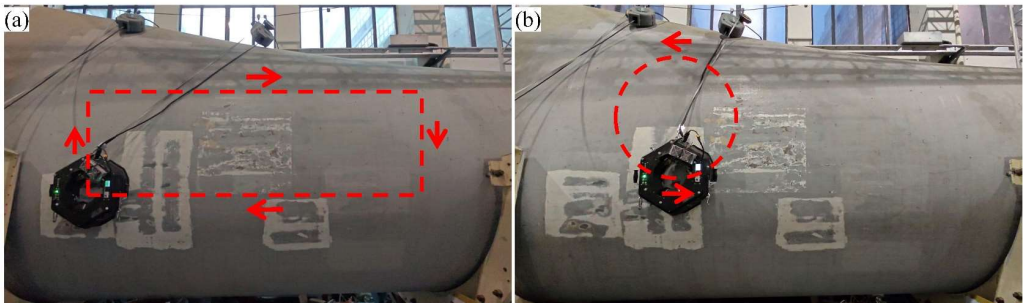

Figure 17. Trajectory diagram on the wind turbine blade. (**a**) A rectangle trajectory with a length of 2.5 m and a width of 1 m. (**b**) A circle trajectory with a diameter of 1 m.

The desired and actual trajectories in the tracking process on the thin-walled skin and wind turbine blade are shown in Figures 18 and 19. Table 2 provides the root mean square error (RMSE) and maximum error for trajectory tracking using the feedforward and proportional–integral controllers on the thin-walled skin and wind turbine blade. The RMSE for all four sets of experiments is below 5 mm, which indicates high trajectory tracking precision.

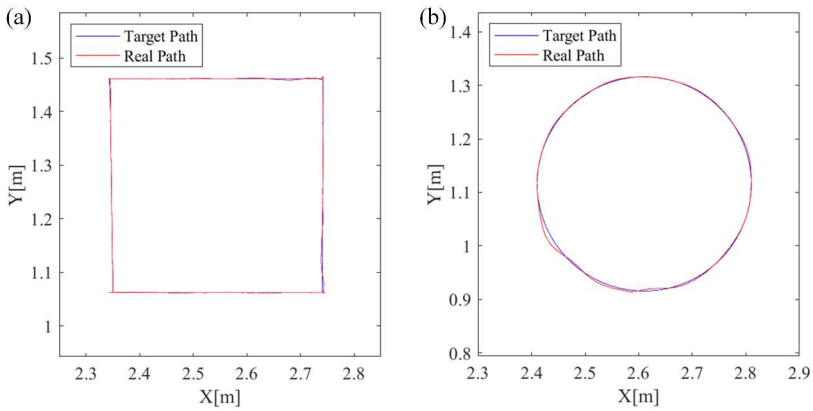

Figure 18. Trajectory tracking on thin-walled skin, target path (blue) and actual path (red). (**a**) A square trajectory with a side length of 0.4 m. (**b**) A circle trajectory with a diameter of 0.4 m.

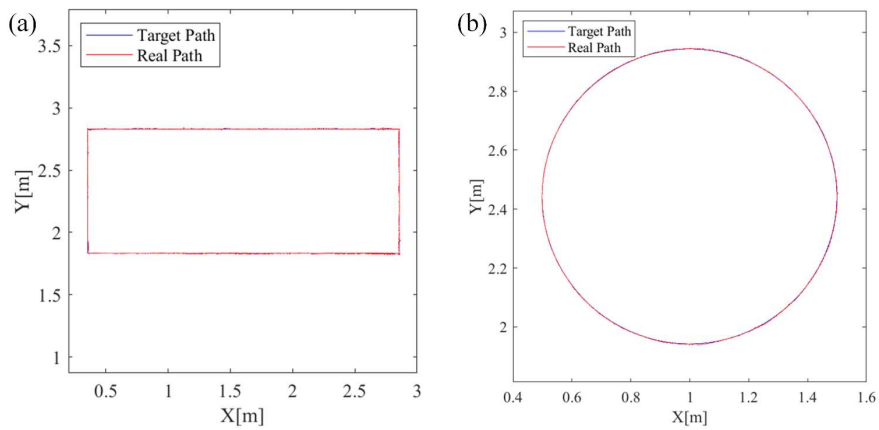

Figure 19. Trajectory tracking on wind turbine blade, target path (blue) and actual path (red). (**a**) A rectangle trajectory with a length of 2.5 m and a width of 1 m. (**b**) A circle trajectory with a diameter of 1 m.

Table 2. RMSE and maximum error for trajectory tracking on thin-walled skin and wind turbine blade using feedforward and proportional–integral controllers.

	Thin-Walled Skin (Straight)	Thin-Walled Skin (Curved)	Wind Turbine Blade (Straight)	Wind Turbine Blade (Curved)
RMSE [mm]	1.1	3.2	2.2	2.3
Maximum Error [mm]	4.7	12.8	16.2	16.8

4.4. Discussion

In the application of climbing robots, a significant adsorption force is required to ensure the robot's movement on curved surfaces. Due to the nature of the curved surfaces, the contact between the driving wheels and the surface is not complete tread-to-plane contact but rather a point contact. These characteristics pose challenges to the robot's movement on curved surfaces. Effectively reducing the driving force under these conditions, while ensuring stable movement, is a feasible solution.

From the experimental results, it can be seen that the proposed AISW mechanism effectively reduces the rotational resistance encountered by traditional ISWs during steering, validating the theoretical analysis presented in Section 2.1 and demonstrating the superiority of the AISW. Additionally, trajectory tracking experiments on different curved surfaces, such as thin-walled skins and actual wind turbine blades, confirm the effectiveness of this motion mechanism in practical applications. This provides new insights for the design and motion control of climbing robots.

We also recognize that incorporating a suspension mechanism that adapts to surface curvature could further enhance the robot's performance, which will be the focus of our future research.

5. Conclusions

This paper proposes the AISWs for climbing robots, where the steering is assisted by the driving wheel, converting sliding friction into rolling friction. The in-place rotation experiments demonstrated that the steering motor current significantly decreased with the use of AISW, to less than half that of traditional symmetrical ISWs, confirming its excellent steering capabilities. A tracking control based on feedforward and proportional–integral (PI) feedback method suitable for the climbing robot with AISWs moving on curved surfaces was then designed. It achieved high-precision trajectory tracking with a root mean square error (RMSE) of less than 5 mm, verifying the effectiveness of AISWs in practical applications.

The employment of AISWs is expected to expand the reachable range of climbing robots and improve trajectory tracking accuracy thus promoting their application in the machining of large and complex components, such as the grinding of wind turbine blade by carrying and equipping the grinding actuator [22]. Additionally, AISWs can be used not only for climbing robots but also for mobile robots operating under heavy load or on curved surface conditions.

Author Contributions: Conceptualization, M.L., X.L. and Z.G.; methodology, M.L. and X.L.; validation, L.X., K.T., and Z.G.; investigation, M.L., X.L., J.H. and Z.G.; resources, L.X. and Z.G.; writing—original draft preparation, M.L. and X.L.; writing—review and editing, K.T. and Z.G.; supervision, Z.G.; project administration, L.X. and Z.G. All authors have read and agreed to the published version of the manuscript.

Funding: This research was supported in part by the National Natural Science Foundation of China under Grant 52375013, and in part by Innovation Fund project of the National Commercial Aircraft Manufacturing Engineering Technology Research Center COMAC-SFGS-2022-2023.

Data Availability Statement: The original contributions presented in the study are included in the article, further inquiries can be directed to the corresponding author/s.

Conflicts of Interest: Author Meifeng Lv and Lei Xue are employed by the company COMAC Shanghai Aircraft Manufacturing Co., Ltd. The remaining authors declare that the research was conducted in the absence of any commercial or financial relationships that could be construed as a potential conflict of interest.

References

1. Tao, B.; Gong, Z.; Ding, H. Robotic cluster machining: Manufacturing revolution for large and complex components. *Sci. China Technol. Sci.* **2022**, *65*, 2215–2217. [CrossRef]
2. Tao, B.; Gong, Z.; Ding, H. Climbing robots for manufacturing. *Natl. Sci. Rev.* **2023**, *10*, nwad042. [CrossRef] [PubMed]
3. Ramalingam, B.; Manuel, V.H.; Elara, M.R.; Vengadesh, A.; Lakshmanan, A.K.; Ilyas, M.; James, T.J.Y. Visual Inspection of the Aircraft Surface Using a Teleoperated Reconfigurable Climbing Robot and Enhanced Deep Learning Technique. *Int. J. Aerosp. Eng.* **2019**, *2019*, 5137139. Available online: https://www.hindawi.com/journals/ijae/2019/5137139/ (accessed on 5 April 2024). [CrossRef]
4. Kermorgant, O. A magnetic climbing robot to perform autonomous welding in the shipbuilding industry. *Robot. Comput. -Integr. Manuf.* **2018**, *53*, 178–186. [CrossRef]
5. Franko, J.; Du, S.; Kallweit, S.; Duelberg, E.; Engemann, H. Design of a Multi-Robot System for Wind Turbine Maintenance. *Energies* **2020**, *13*, 2552. [CrossRef]
6. Bisht, R.S.; Pathak, P.M.; Panigrahi, S.K. Design and development of a glass façade cleaning robot. *Mech. Mach. Theory* **2022**, *168*, 104585. [CrossRef]
7. Zhong, Z.; Xu, M.; Xiao, J.; Lu, H. Design and Control of an Omnidirectional Mobile Wall-Climbing Robot. *Appl. Sci.* **2021**, *11*, 11065. [CrossRef]
8. Liu, J.-H.; Padrigalan, K.E. The Kinematic Analysis of a Wind Turbine Climbing Robot Mechanism. *Appl. Sci.* **2022**, *12*, 1210. [CrossRef]
9. Huang, H.; Li, D.; Xue, Z.; Chen, X.; Liu, S.; Leng, J.; Wei, Y. Design and performance analysis of a tracked wall-climbing robot for ship inspection in shipbuilding. *Ocean Eng.* **2017**, *131*, 224–230. [CrossRef]
10. Guo, T.; Liu, X.; He, T.; Song, D. Synchro-Drive-Based Underwater Climbing Adsorption Robot. *IEEE Robot. Autom. Lett.* **2022**, *7*, 6250–6257. [CrossRef]
11. Eto, H.; Asada, H.H. Development of a Wheeled Wall-Climbing Robot with a Shape-Adaptive Magnetic Adhesion Mechanism. In Proceedings of the 2020 IEEE International Conference on Robotics and Automation (ICRA), Paris, France, 31 May–31 August 2020; pp. 9329–9335.
12. Fiorello, I.; Tricinci, O.; Naselli, G.A.; Mondini, A.; Filippeschi, C.; Tramacere, F.; Mishra, A.K.; Mazzolai, B. Climbing Plant-Inspired Micropatterned Devices for Reversible Attachment. *Adv. Funct. Mater.* **2020**, *30*, 2003380. [CrossRef]
13. Bae, B.; Lee, D.-H. Design of a Four-Wheel Steering Mobile Robot Platform and Adaptive Steering Control for Manual Operation. *Electronics* **2023**, *12*, 3511. [CrossRef]
14. Li, K.; Bao, L.; Han, C.; Shin, K.; Kim, W. IMU-based Online Kinematic Model Parameter Estimation for Four-Wheeled Skid-Steering Mobile Robot Desired Motion Tracking on Different Terrains. In Proceedings of the 2022 22nd International Conference on Control, Automation and Systems (ICCAS), Jeju, Republic of Korea, 27 November–1 December 2022; pp. 950–954.
15. Xu, L.; Yang, Y.; Chen, Q.; Fu, F.; Yang, B.; Yao, L. Path Tracking of a 4WIS–4WID Agricultural Machinery Based on Variable Look-Ahead Distance. *Appl. Sci.* **2022**, *12*, 8651. [CrossRef]

16. Xu, H.; Tan, D.W.; Zhang, Z.Y.; Xue, K.; Luan, Y.K.; Peng, G.L. Configuration Design of a Novel Mobile Robot with 5th Wheel. *Key Eng. Mater.* **2010**, *419–420*, 605–608.
17. Ding, T.; Zhang, Y.; Ma, G.; Cao, Z.; Zhao, X.; Tao, B. Trajectory tracking of redundantly actuated mobile robot by MPC velocity control under steering strategy constraint. *Mechatronics* **2022**, *84*, 102779. [CrossRef]
18. Liu, X.; Wang, W.; Li, X.; Liu, F.; He, Z.; Yao, Y.; Ruan, H.; Zhang, T. MPC-based high-speed trajectory tracking for 4WIS robot. *ISA Trans.* **2022**, *123*, 413–424. [CrossRef] [PubMed]
19. Kato, T.; Watanabe, K.; Maeyama, S. Image-based fuzzy trajectory tracking control for four-wheel steered mobile robots. *Artif. Life Robot.* **2012**, *17*, 130–135. [CrossRef]
20. Tan, S.; Wang, Y.; Cheng, W.; Luo, T.; Zhang, N.; Li, S.; Pan, B.; Cui, X. Cascade direct yaw moment control for an independent eight in-wheel motor-driven autonomous vehicle. *Electronics* **2022**, *11*, 2930. [CrossRef]
21. Gao, G.; Qin, Q.; Chen, S. Turning control of a mobile robot for greenhouse spraying based on dynamic sliding mode control. *Int. J. Adv. Robot. Syst.* **2017**, *14*, 1729881417744754. [CrossRef]
22. Shi, Y.; Gong, Z.; Tao, B.; Li, K.; Gu, Z.; Tan, K.; Ding, H.A. A Climbing Machining Robot for Large Components with Variable Curvature Surface. *IEEE/ASME Trans. Mechatron.* 2024; *early access*. [CrossRef]

Disclaimer/Publisher's Note: The statements, opinions and data contained in all publications are solely those of the individual author(s) and contributor(s) and not of MDPI and/or the editor(s). MDPI and/or the editor(s) disclaim responsibility for any injury to people or property resulting from any ideas, methods, instructions or products referred to in the content.